The effect of rock permeability and porosity on seismoelectric conversion: experiment and analytical modelling

Rong Peng[1, 2], Bangrang Di[1], Paul Glover[2], Jianxin Wei[1], Piroska Lorinczi[2], Pinbo Ding[1], Zichun Liu[1], Yuangui Zhang[1], Mansheng Wu[3]

1 College of Geophysics and information engineering, China University of Petroleum (Beijing), China

2 School of Earth and Environment, University of Leeds, UK

3 BGP INC., China National Petroleum Corporation

Rong Peng: hnpengrong@163.com

Bangrang Di: cupdbr@126.com

Paul Glover： P.W.J.Glover@leeds.ac.uk

Jianxin Wei: weijx@cup.edu.cn

Piroska Lorinzi: P.Lorinczi@leeds.ac.uk

Pinbo Ding: dingpinbo@163.com

Zichun Liu： liuzichun111@163.com

Yuangui Zhang： 1304056865@qq.com

Mansheng Wu: wumansheng@163.com

Abstract

The seismoelectric method is a modification of conventional seismic measurements which involves the conversion of an incident poroelastic wave to an electromagnetic signal that can be measured at the surface or down a borehole. This technique has the potential to probe the physical properties of the rocks at depth. The problem is that we currently know very little about the parameters which control seismoelectric conversion and their dependence on frequency and permeability, which limits the development of the seismoelectric method. The seismoelectric coupling coefficient indicates the strength of seismoelectric conversion. In our study, we focus on the effects of the reservoir permeability, porosity and frequency on the seismoelectric coupling coefficient through both experimental and numerical modelling. An experimental apparatus was designed to record the seismoelectric signals induced in water-saturated samples in the frequency range from 1 kHz to 500 kHz. The apparatus was used to measure seismoelectric coupling coefficient as a function of porosity and permeability. The results were interpreted using a micro-capillary model for the porous medium to describe the seismoelectric coupling. The relationship between seismoelectric coupling coefficients and the permeability and porosity of samples were also examined theoretically. The combined experimental measurements and theoretical analysis of the seismoelectric conversion has allowed us to ascertain the effect of increasing porosity and permeability on the seismoelectric coefficient. We found a general agreement between the theoretical curves and the test data, indicating that seismoelectric conversion is enhanced by increases in porosity over a range of different frequencies. However, seismoelectric conversion has a complex relationship with rock permeability, which changes with frequency. For the low-permeability rock samples ($0\text{-}100\times10^{-15}$ m^2), seismoelectric coupling strengthens with the increase of permeability logarithmically in the low frequency range (0-10 kHz); in the high frequency range (10-500 kHz), the seismoelectric coupling is at first enhanced, with small increases of permeability leading to small increases in size in electric coupling. However, continued increases of permeability then lead to a slight decrease in size and image conversion again. For the high-permeability rock samples (300×10^{-15} m^2 - 2200×10^{-15} m^2), the seismoelectric conversion shows the same variation trend with low-permeability samples in low frequency range; but it monotonically decreases with permeability in the high frequency range. The experimental and theoretical results also indicate that seismoelectric conversion seems to be more sensitive to the changes of low-permeability samples. This observation suggests that seismic conversion may have advantages in characterizing low permeability reservoirs such as tight gas and tight oil reservoirs and shale gas reservoirs.

Key words: porosity, permeability, seismoelectric conversion, coupling coefficients, frequency dependent

Introduction

The passage of poroelastic waves through a porous media, such as a rock, sets up local fluid flows, and those flows lead to the generation of an electrical potential (e.g., Walker et al. 2014). This coupling of poroelastic waves and electrical potential generation is called the seismoelectric effects, and its size is characterised by the streaming potential coefficient, C_{sp} (also called the seismoelectric coupling coefficient, *L(w)*). The seismoelectric effects have been investigated by experimental research and numerical modelling on various rock models (Glover & Jackson 2009; Bordes et al. 2009; Schakel et al. 2011a, 2011b, 2011c, 2012; Sénéchal & Bordes 2012; Jougnot et al. 2013; Roubinet et al. 2016). The streaming potential coefficient *L(w)* depends on the microstructural and transport properties of the porous media, or in our case, the rocks that compose the reservoir (e.g., Revil et al. 1999; Glover et al. 2010).

Different theoretical models of the streaming potential coefficient have been proposed. Packard (1953) presented a model for the frequency-dependent streaming potential coefficient for capillary tubes. Pride (1994) proposed the seismoelectric coupling coefficient for porous medium. Reppert et al. (2001) revised the Packard model by using the low- and high-frequency approximations of the Bessel functions, which is almost the same with the model of Packard. Since the streaming potential is induced at the solid-fluid phase, the surface conductivity of the solid surface affect this electric potential, and the surface conductivity of the rock has impact on the apparent effect of the permeability (Jouniaux et al. 2000). Jouniaux and Bordes (2012) summarized the experiments and theories of frequency-dependent streaming potential and indicated that the transition frequency was dependent of the permeability. It has also been recognised that the seismoelectric coupling coefficient is a function of permeability and porosity (Jouniaux & Pozzi 1995), thus the rock properties can be inferred from the seismoelectric conversion. However, the relationships between porosity, permeability and *L(w)* have not been studied in sufficient depth for their exact forms to be known. It is impossible to discuss permeability and porosity separately since these two parameters are interdependency properties of rocks. Permeability of porous media is usually expressed as function of some physical properties of the interconnected pore system such as porosity (Dullien, 1979). Because of complexity of the pore channels, few simple functions can exist. If the relationship between porosity, permeability and *L(w)* can be well understood, there is potential for using measurements of *L(w)* from seismoelectric field measurements (Thompson et al. 2007; Dupuis et al. 2009) to obtain a reservoir's porosity and permeability, offering an alternative method for providing these critical values which does not depend on drilling wells or analysing cores.

The streaming potential and electro-osmotic pressure on sandstones, limestones and glass bead samples in the low frequency range (0-100 Hz) were measured by Jouniaux and Pozzi (1995) and Pengra (1999). Their results indicated that the fluid permeability of the material is also related to electro-kinetic effects. This has been confirmed for steady-state streaming potential and permeability measurements by Glover et al. (2006), and lead to the RGPZ model for permeability prediction. It was subsequently generalised by Walker and Glover (2010) in a study of characteristic length scales and scaling constants in fluid permeability prediction, and also to a link between time-dependent electro-kinetic coupling and fluid permeability.

Meanwhile, Mikhailov et al. (2000) detected the Stoneley-wave-induced electric field in a borehole (150 Hz centre frequency), and showed that borehole electro-seismic measurements could be used to characterize permeable zones. Since it was becoming clear that frequency-dependent *L(w)* was needed to process and understand seismoelectric field data, it was thought necessary to make well-controlled measurements of *L(w)* as a function of frequency in the laboratory. Several frequency-dependent *L(w)* measurement apparatuses were designed and built for use in the frequency range 1 Hz to 1 kHz by applying a harmonically varying flow (Tardif et al. 2011; Glover et al. 2012a; Glover et al. 2012b), whose results have shown a clear relationship between transition frequency, grain size and steady-state fluid permeability. The laboratory measurements of the streaming potential properties of minerals was performed by Morgan et al. (1989) , results indicated that the anomalies of the streaming potential can be used to predict the earthquake phenomena. Schoemaker et al. (2007, 2008) measured the streaming potential and dynamic permeability by using a Dynamic Darcy Cell (DCC) with a mechanical shaker in the range from 5 to 200 Hz. but the permeability is given by Darcy's law, which does not reflect the permeability through the potential acquired by seismoelectric measurements, and the relationship between permeability and seismoelectric coupling has not been studied. Independently, Wang et al. (2010) analysed the relationship between the permeability and streaming potential of rocks in low frequency range (0-70 Hz), indicating that *L(w)* has a strong predictive relationship with conventional gas permeability, while Luong and Sprik (2013) carried out streaming potential and electro-osmosis measurements (100 Hz -100 kHz) to characterize the zeta potential and the average pore size of porous materials on 6 unconsolidated samples. Schoemaker et al. (2012) experimentally validated a electrokinetic formulation of the streaming potential of Pride (1994). The streaming potential is measured in a frequency band ranging from 5Hz up to 150 Hz, and the numerical modelling use a frequency of 500 kHz. Guan et al. (2013) proposed a method of obtaining reservoir permeability using the seismoelectric well logging data of a fluid-saturated porous formation using data in the frequency range 0 Hz -2 kHz, finding that the amplitude ratio of the converted electric field to the pressure (what he called the REP, but which is formally the same as *L(w)* is sensitive to porosity, while the tangent of the REP’s phase is sensitive to permeability. Zhu et al.

(2015) performed seismoelectric experiments on a porous quartz-sand sample with anisotropic permeability (20 kHz to 90 kHz) and showed that *L(w)* depends directly on permeability, inferring that the amplitudes of measured seismoelectric signals may, in principle, be used to determine the permeability in a given formation. Furthermore they also measured seismoelectric anisotropy and found that it is correlated with a sample's anisotropic permeability.

Though the rock properties (permeability, porosity, etc.) have been investigated based on seismoelectric conversion and qualitative results have been acquired from the previous research, the settled relationship to describe the interdependence of *L(w)* and permeability still needs to be identified more clearly. This is especially true at the higher frequencies because most research has been carried out at low-frequencies (less than 2 kHz in the above references). Luong and Sprik (2013) and Zhu et al. (2015) have made measurements of electro-kinetic parameters in the 'high' frequency range (but to less than 100 kHz). Luong and Sprik (2013) focused on determining the zeta potential and pore size by seismic methods and did not take account of porosity and permeability, while Zhu et al. (2015) pointed out that the rock permeability is related directly to seismoelectric signals, but did not provide the formal relationship between permeability and seismoelectric conversion coefficients.

In this study, we have performed seismoelectric measurements of rock samples as a function of porosity and permeability using natural and artificial samples at three different frequencies (1 kHz, 10 kHz and 500 kHz, we define 0-10 kHz as the low frequency range and 10 kHz-500 kHz as the high frequency range in this paper). The full theoretical relationship between *L(w)*, permeability and porosity has been calculated based on a micro-capillary model of porous media. We give out the effect of permeability on transition frequency, which indicates that the transition frequency is inversely related to permeability. And the change of transition frequency leads to the complicated relationship between the permeability and *L(w)* divided into low frequency and high frequency ranges. In addition, we present the quantitative relationship between *L(w)* and permeability for a constant porosity with numerical and experimental data for the first time, including the dependence of *L(w)* on both high permeability and low permeability rocks. This work now gives us experimental evidence for the variation of seismoelectric coupling for rock samples as a function of frequency, porosity and permeability, as well as providing a validated theoretical model for seismoelectric coupling for rock samples as a function of frequency, porosity and permeability.

Experimental method and samples

A schematic of the apparatus for measuring *L(w)* is shown in Figure 1. The apparatus operates in a water tank (200×150×100 cm) (Zhu et al., 2008; Schakel et al., 2011a, 2011b, 2011c; Peng et al. 2016; 2017). A compressional wave (*P*-wave) piezoelectric transducer is used as the seismic source. The resulting *P*-wave propagates through fully saturated rock samples causing a local travelling pressure disturbance, which perturbs the electric double layer (EDL). This perturbation leads to a polarisation of charge which gives rise to a measureable macroscopic streaming potential across the porous medium, and which can be measured as an electric signal by the electrodes shown in Figure 1.

In our study, we only consider the P-wave in our experiment and theory, and the P-wave converted S-waves when the P-wave hit the rock sample are considered to be ignored. Because (1) the P-waves in our experiment are nearly perpendicular incident, hence, the conversion to shear waves is not strong; (2) shear waves cannot propagate in fluids, so we think the converted shear wave is very weak even though the conversion happens; (3) the weak shear waves cannot induce the enough strong seismoelectric conversion which can be detected in our experiment. Because according to our results, the P-wave induced SE signals recorded in our experiment is not that strong, let along the S-wave induced SE signals.

The fluid in the water tank is an aqueous solution of NaCl with a concentration of 1.5 g/dm^3, the corresponding conductivity of the fluid is 0.24S/m, which is measured with conductivity meter. Two gauze Ag/AgCl disc electrodes with a diameter of 2 cm (V1 and V2) and two pressure transducers (P1 and P2) are placed on each side of the rock sample (touching the rock samples) to record the seismoelectric signal and the acoustic signal, respectively. Both of the two electrode potentials (V1 and V2) are given relative to the common ground. And the two electrodes touch the rock samples when measurements are performed, so the measured SE signals are the coseismic fields in this paper (Peng et al. 2017). The instantaneous seismoelectric (streaming) potential ΔV is obtained by taking the difference between the potentials of the electrodes on each side of the rock sample (ΔV=V1-V2). The transient pressure difference, ΔP, across the sample at any instant is obtained by taking the difference of the measurements made by transducers P1 and P2 (ΔP=P1-P2). The ratio of ΔV/ΔP is the experimental value of the *L(w)* of the rock sample (Zhu et al., 2008).

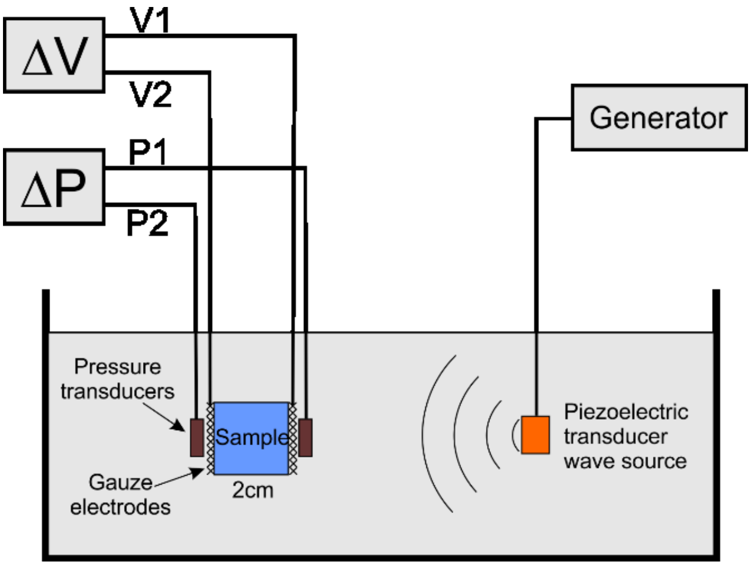

Figure 1. Schematic diagram of the seismoelectric apparatus.

Seismoelectric measurements were made on 28 natural rock samples (cylindrical core plugs with a length of 2 cm and a diameter of 2 cm) and 4 artificial fractured samples with controlled crack densities (cubic, 2×2×2 cm). The 28 natural samples include 6 granites and 22 sandstones and can be considered as isotropic samples, with a range of permeabilities from 0.001×10^{-15} m^2 to 69.488×10^{-15} m^2 and porosities from 9.91% to 16.3%, as shown in Table 1. The porosity is effective porosity acquired by helium porosimetry measurements. The gas volume method is used for determination of porosity according to Boyle's law. The artificial fractured samples were prepared using the manufacturing process described in Ding et al. (2013), Ding et al. (2014a; 2014b) and Zhu et al. (2015). The sand minerals and polymer materials as cracks are placed into the mould, and after the sample prepared in the mould, it was left to dry in a constant temperature oven for weeks. The sample was sintered in a furnace and the high molecular material discs were then decomposed and drained out, leaving voids as fractures. The densities of the four artificial samples with induced crack are 0%, 3%, 6%, 9%, respectively. Each has a geometry represented in the schematic diagram shown in Figure 2. Since the volume of the induced cracks is small compared to the volume of the matrix porosity, all of the induced samples can be assumed to have the same porosity, which in our measurements was (23.8±0.5)%.

Despite the change in porosity being insignificant, the induced cracks have a considerable effect on the size and anisotropy of the sample permeability. Measurements made in the three orthogonal directions on the artificial sample with 0% crack density all give the same value because the sample is isotropic. However, the other 3 artificial samples include induced fractures in a preferential direction. Measurements made on these samples in the three orthogonal directions provide three different seismoelectric coupling coefficients, one for each direction, due to the anisotropy of the samples.

Consequently, the 4 cubic samples, each with the same porosity, provide 10 independent *L(w)* measurements, each associated with a different permeability. Figure 3 shows all of the experimental samples used in this work, core samples on the left-hand side, and the induced crack samples on the right-hand side. The presence of cracks can just be observed in these, as indicated in the figure.

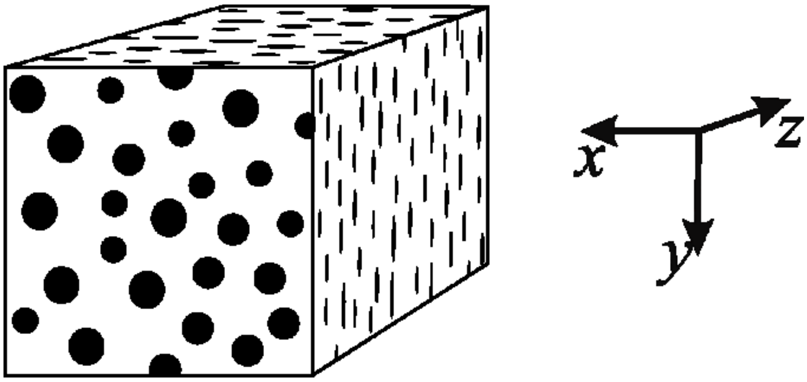

Figure 2. Schematic of the artificial fractured sample. The porosity of all the fractured samples is 23.8%. The cracks are parallel to *xy* plane, and vertical to *xz* and *yz* planes.

(a) (b)

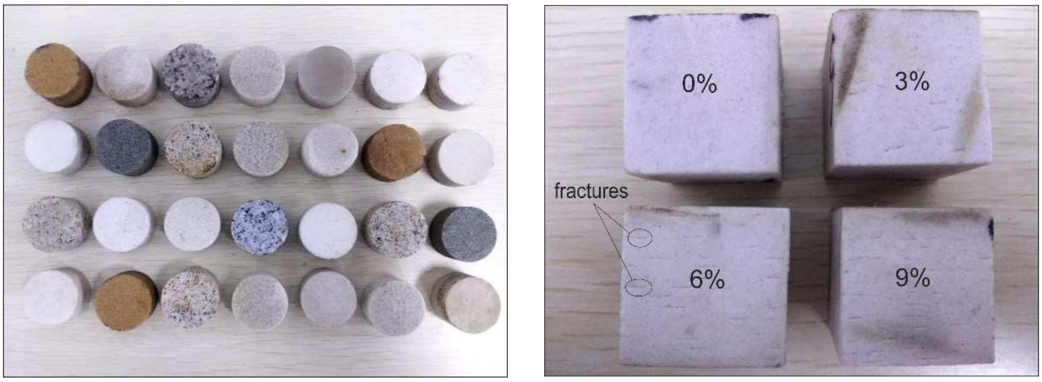

Figure 3. Photos of (a) the 28 natural samples, and (b) the 4 artificial fractured samples, in which the artificial fractures can just be seen.

Table 1. Porosity and permeability of the rock samples used in the study.

Sample Number	Porosity (%)	Permeability ($\times 10^{-15} m^2$)	Sample Number	Porosity (%)	Permeability ($\times 10^{-15} m^2$)
N1	10.84	0.001	N15	11.75	0.263
N2	13.44	0.002	N16	10.88	0.506
N3	12.40	0.004	N17	10.37	0.624
N4	12.15	0.007	N18	12.24	1.192
N5	15.98	0.020	N19	14.11	2.161
N6	10.96	0.023	N20	10.00	3.590
N7	12.16	0.025	N21	12.60	11.450
N8	10.93	0.034	N22	16.30	13.135

N9	13.03	0.079	N23	9.92	13.291
N10	9.91	0.090	N24	12.54	19.090
N11	12.92	0.117	N25	14.20	32.828
N12	13.62	0.122	N26	14.23	48.100
N13	11.29	0.134	N27	16.17	57.400
N14	15.05	0.259	N28	11.94	69.488
A1	23.8	310.79	A3*y*	23.8	1696.30
A2*x*	23.8	847.21	A3*z*	23.8	370.43
A2*y*	23.8	876.10	A4*x*	23.8	2053.27
A2*z*	23.8	325.53	A4*y*	23.8	2164.32
A3*x*	23.8	1509.34	A4*z*	23.8	427.39

Note. Samples labelled N are natural rock samples, and those labelled A are artificial fractured sandstones. A1 is the sandstone without cracks, while the labels x, y and z represent the direction of wave propagation as defined in Figure 3. The porosity is effective porosity acquired by helium porosimetry measurements. Permeability is Klinkenberg-corrected permeability (Klinkenberg 1941).

Theoretical development

This section contains the major theoretical development in this paper. The first subsection references existing work and applies it to the capillary bundle model which we use. Subsequent sections develop the model further in order to obtain the frequency-dependent relationship between permeability, porosity and the seismoelectric coupling coefficient. And the theory we talk about in this paper is only the P-wave field. The seismoelectric measurements can be impacted by the conductivity of the rock surface (Alkafeef & Alajmi 2006; Wang et al. 2015), in order to simplify the situation, we neglect the effects of surface conductivity on the seismoelectric coupling in our theory.

Theory of the electric double layer in porous media

In this work we have modelled porous rock as a parallel aligned bundle of capillary of varying radius. The correspondence between the microscopic parameters of this capillary bundle model (the number of capillaries, n_0, and the capillary radius, r_0) and the macroscopic reservoir parameters (the rock porosity, ϕ, and permeability, k) can be expressed as (Kozeny 1927)

$$\phi = n_0 \pi r_0^2, \text{ and} \tag{1}$$

$$k = \frac{n_0 \pi r_0^4}{8}. \tag{2}$$

The ion concentration distribution of a multi-component electrolyte in a capillary satisfies the Boltzmann equation (Harris 1971)

$$C_i = C_0 \exp\left(\frac{-Z_i e \psi}{k_B T}\right), \tag{3}$$

where C_i is the concentration of component i, C_0 is the initial concentration of the solution, $e=1.6\times 10^{-19}$ is the fundamental charge, n_A is Avogadro number , Z_i is the valence of component i , ψ is a potential function of the distance between the wall of capillary and ions ($\psi(r)$), k_B is Boltzmann constant. T is absolute temperature (in K). The electric density ρ_e for a solution with a symmetric cation-anion of valence Z-Z in a capillary is

$$\rho_e = en_A Z(C_+ - C_-) = 2FZC_0 \sinh(\frac{Ze\psi}{k_B T}). \tag{4}$$

The capillary charge satisfies the Poisson equation (Probstein 1994):

$$\frac{1}{r}\frac{\partial}{\partial_r}\left(r\frac{\partial\psi}{\partial_r}\right) = -\frac{\rho_e}{\varepsilon} = -\frac{en_A}{\varepsilon}\sum_i Z_i C_0 \exp(\frac{-Z_i e\psi}{k_B T}), \tag{5}$$

where ε is the dielectric constant of the solution, r is the coordinate variable along capillary radius of cylindrical coordinates, representing the distance between the center of capillary and ions.

In the Z-Z valence symmetric salt electrolyte solution, Z_i is the valence of component i, Z_i includes Z_+ and Z_-, $Z_+ = Z$; $Z_- = -Z$, and the Poisson equation can be rewritten as

$$\frac{1}{r}\frac{\partial}{\partial_r}\left(r\frac{\partial\psi}{\partial_r}\right) = -\frac{en_A}{\varepsilon}\sum_i Z_i C_0 \exp\left(\frac{-Z_i e\psi}{k_B T}\right) = \frac{2en_A ZC_0}{\varepsilon}\sinh(\frac{Ze\psi}{k_B T}). \tag{6}$$

If the thickness of the EDL, d, is much smaller than the capillary radius r_0 ($r_0 \gg d$), Φ is very small over the internal area of the capillary. Hence, we have

$$\sinh\frac{Ze\psi}{k_B T} \approx \frac{Ze\psi}{k_B T}. \tag{7}$$

The Poisson equation can then be simplified as

$$\frac{1}{r}\frac{\partial}{\partial_r}\left(r\frac{\partial\psi}{\partial_r}\right) = -\frac{\rho_e}{\varepsilon} = \frac{2en_A ZC_0}{\varepsilon}\sinh\left(\frac{Ze\psi}{k_B T}\right) = \frac{\psi}{(d^2)}, \tag{8}$$

where: $d = \sqrt{\frac{\varepsilon k_B T}{2e^2 Z^2 n_A C_0}}$.

Substituting the following boundary conditions into equation 8 : $r = 0, \frac{\partial\psi}{\partial_r} = 0$; $r = r_0, \psi = \zeta$, ζ is the zeta potential of electric double layer. Then the solution of the potential distribution in equation 8 can be obtained as

$$\psi = \zeta\exp(-\frac{r_0 - r}{d}). \tag{9}$$

In this work we calculate the zeta potential using the empirical equation (Pride & Morgan, 1991). We assume that the zeta potential could be constant with the concentration (Fiorentino et al. 2016), also we assume that the zeta potential is the same for all the natural samples since the fluid concentration is not changed in this study.

$$\zeta = 0.008 + 0.026 log_{10}^{C_0}. \tag{10}$$

However, if a more analytical approach is required, a fully theoretical treatment of the zeta potential has been published (Glover and Déry, 2010; Glover et al., 2012a, 2012b) and validated on a large database of experimental measurements (Walker and Glover, 2018; Glover 2018).

The ion concentration distribution given as Equation (3), can be written as

$$C_i = C_0 \exp(\frac{-Z_i e\psi}{k_B T}) = C_0 \sum_{n=0}^{\infty} \frac{(-Ze\zeta)^n}{(k_B T)^n\, n!} \exp[-\frac{n(r_0 - r)}{d}] \tag{11}$$

using Taylor series expansion. C_i includes C_+ and C_- :

$$C_+ = C_0 \exp(\frac{-Ze\psi}{k_B T}), \tag{12}$$

$$C_- = C_0 \exp(\frac{Ze\psi}{k_B T}). \tag{13}$$

Frequency-dependent hydraulic flow velocity with electro-kinetic influence

Assuming that the porous fluid satisfies the convective form of the incompressible Navier-Stokes equation with an electro-kinetic external source (Deissler 1976)

$$\eta \nabla^2 \boldsymbol{u} - \rho_f \left[\frac{\partial \boldsymbol{u}}{\partial t} + (\boldsymbol{u} \cdot \nabla)\boldsymbol{u}\right] = \nabla P - \rho_e \boldsymbol{E}, \tag{14}$$

where ρ_f is the fluid density, P is the fluid pressure, $\boldsymbol{u}$ is the flow velocity, and η is the fluid viscosity. The electric field intensity $\boldsymbol{E} = -\nabla U$ in the quasi-static limit of the Maxwell equations, where U is the streaming potential (Revil et al., 2015).

In our capillary model, fluid flow is incompressible and constrained to the *z*-direction. Hence, $\nabla \cdot \boldsymbol{u} = 0$, $\boldsymbol{u} = u_z \boldsymbol{e}_z$, where $\boldsymbol{e}_z$ is the unit vector in the capillary axial direction, such that we may write $\frac{\partial \boldsymbol{u}(r,z)}{\partial z} = 0$. Therefore, u_z is a function of r, and $(\boldsymbol{u} \cdot \nabla)\boldsymbol{u}$ in the Navier-Stokes equation can be ignored.

In the following analysis, there are certain further assumptions: (i) that the pressure gradient of an pressure wave field in the *z*-direction of the porous medium is $\frac{\partial P(z,t)}{\partial z}$, (ii) that the pressure field is harmonic, $P = P_0 e^{-i\omega t}$, $\omega = 2\pi f$, (iii) that the pressure induced streaming potential is also harmonic, $U = U_0 e^{-i\omega t}$, (iv) that fluid flow is incompressible, so $\nabla \cdot \boldsymbol{u} = 0$, and (v) non-homogenous vibration of the solid-fluid interface caused by pressure waves can be ignored. Under these conditions, the Navier-Stokes equation can be expressed as

$$\nabla^2 \boldsymbol{u} + K^2 \boldsymbol{u} = \frac{1}{\eta}(\nabla P + \rho_e \nabla U) , \tag{15}$$

where $K^2 = \frac{i\omega\rho_f}{\eta}$.

Then substituting Equation (4) into this equation and multiplying both sides by r^2 gives

$$r\frac{\partial}{\partial r}\left(r\frac{\partial \boldsymbol{u}}{\partial r}\right) + K^2 r^2 \boldsymbol{u} = \frac{r^2}{\eta}\frac{\partial P}{\partial z} - \frac{2r^2 e n_A Z C_0}{\eta}\sinh\left(\frac{Ze\psi}{k_B T}\right)\frac{\partial U}{\partial z}. \tag{16}$$

When this equation is compared with the definition of a Bessel equation, when $K^2 \neq 0$, and taking account of the boundary condition: (at $r = 0$, $\boldsymbol{u}$ has a non-zero limited value and at $r = r_0$, $\boldsymbol{u} = 0$) we can obtain the solution of Equation (16) as

$$\boldsymbol{u}(\boldsymbol{r}) = \frac{1}{K^2\eta}\left[1 - \frac{J_0(Kr)}{J_0(Kr_0)}\right]\frac{\partial P}{\partial z} + \frac{\varepsilon\zeta}{\eta(1+K^2 d^2)}\left[\frac{J_0(Kr)}{J_0(Kr_0)} - e^{\frac{r_0 - r}{d}}\right]\frac{\partial U}{\partial z} \tag{17}$$

This is the distribution of the fluid velocity in the capillary, and $J_0(Kr) = \sum_{m=0}^{\infty}\frac{(-1)^m}{(m!)^2}\left(\frac{Kr}{2}\right)^{2m}$ is the zero order Bessel function of the first kind.

Frequency-dependent electrical flow with hydraulic flow influence

The molar flux of component i, in a dilute solution, is (Probstein 1994)

$$q_i = -v_i Z_i C_i \frac{\partial U}{\partial z} + C_i \boldsymbol{u}\,, \tag{18}$$

where v_i is the ionic mobility of component i. The value of C_i is given by Equation (3). The distribution of fluid velocity $\boldsymbol{u}$ in the capillary is given by Equation (17). The molar flux is the sum of the contribution of ionic migration and diffusion. The first term of Equation (18) is the molar flux caused by ion migration in an electric field; and the second term indicates the molar flux caused by ion diffusion. The second term relates to the fluid velocity in the capillary which mainly includes the flow caused by pressure and the flow velocity caused by the forced diffusion of the fluid particles in the electric field, i.e., Equation (17). Therefore, the flux of the ionic diffusion is mainly composed of the flux generated by the diffusion of the fluid ions induced by the pressure and the molar flux generated by the forced diffusion of the ions under the electric field.

$$q_i = -v_i Z_i C_i \frac{\partial U}{\partial z} + \frac{C_i}{K^2\eta}\left[1 - \frac{J_0(Kr)}{J_0(Kr_0)}\right]\frac{\partial P}{\partial z} + \frac{C_i \varepsilon \zeta}{\eta(1+K^2d^2)}\left[\frac{J_0(Kr)}{J_0(Kr_0)} - e^{\frac{r_0-r}{d}}\right]\frac{\partial U}{\partial z}\,. \tag{19}$$

Integrating this equation along the capillary cross-section, the ion current density of component i for one capillary is

$$w_i = \int_0^{r_0} q_i(r) 2\pi r \mathrm{d}r. \tag{20}$$

For a parallel aligned capillary bundle model, the ion current density per unit area is $W_i = n_0 w_i$. We can obtain the total ion current density per unit area by integration over the radius of the capillary tube, as

$$W_i = n_0 \int_0^{r_0} q_i(r) 2\pi r \mathrm{d}r, \tag{21}$$

to give

$$W_i = 2\pi n_0 \begin{bmatrix} \int_0^{r_0} -v_i Z_i C_i r\mathrm{d}r \frac{\partial U}{\partial z} + \int_0^{r_0} \frac{C_i}{K^2\eta}\left[1 - \frac{J_0(Kr)}{J_0(Kr_0)}\right] r\mathrm{d}r \frac{\partial P}{\partial z} \\ + \int_0^{r_0} \frac{C_i \varepsilon \zeta}{\eta(1+K^2d^2)}\left[\frac{J_0(Kr)}{J_0(Kr_0)} - e^{\frac{r_0-r}{d}}\right] r\mathrm{d}r \frac{\partial U}{\partial z} \end{bmatrix} \tag{22}$$

According to the definition of electric current density, the electric current density in capillary, I, is (Bockris & Reddy 1970)

$$I = \sum_i e n_A Z_i q_i\,. \tag{23}$$

Integrating this equation over the capillary cross-section, the electric current density of the whole capillary bundle can be expressed as

$$j = e n_A Z (W_+ - W_-)\,, \tag{24}$$

or,

$$j = e n_A Z\left(n_0 \int_0^{r_0} q_+(r) 2\pi r \mathrm{d}r - n_0 \int_0^{r_0} q_-(r) 2\pi r \mathrm{d}r\right) = F Z n_0 \int_0^{r_0} [q_+(r) - q_-(r)] 2\pi r \mathrm{d}r. \tag{25}$$

This equation can be rewritten as

$$j = -L(\omega)\frac{\partial P}{\partial z} - \sigma(\omega)\frac{\partial U}{\partial z}\,, \tag{26}$$

where

$$L(\omega) = -2\pi e n_A Z n_0 \left[\int_0^{r_0} \frac{C_+}{K^2\eta}\left[1 - \frac{J_0(Kr)}{J_0(Kr_0)}\right] \mathrm{rdr} - \int_0^{r_0} \frac{C_-}{K^2\eta}\left[1 - \frac{J_0(Kr)}{J_0(Kr_0)}\right] \mathrm{rdr}\right], \tag{27}$$

$$\alpha = 2\pi e n_A Z n_0 \left[\int_0^{r_0} v_+ Z_+ C_+ rdr - \int_0^{r_0} v_- Z_- C_- rdr\right], \text{ and}$$

(28)

$$\beta = -2\pi e n_A Z n_0 \left[\int_0^{r_0} \frac{C_+ \varepsilon\zeta}{\eta(1+K^2d^2)}\left[\frac{J_0(Kr)}{J_0(Kr_0)} - e^{\frac{r_0-r}{d}}\right] \mathrm{rdr} + \int_0^{r_0} \frac{C_- \varepsilon\zeta}{\eta(1+K^2d^2)}\left[\frac{J_0(Kr)}{J_0(Kr_0)} - e^{\frac{r_0-r}{d}}\right] \mathrm{rdr}\right] \tag{29}$$

and, (30)

The term $\sigma(\omega)\frac{\partial U}{\partial z}$ is the electric conducting current caused by the movement of charged particles themselves (including ion migration and ion diffusion). $\sigma(\omega)$ is defined as the composite conductivity, with α and β representing the coefficient of the electric current produced by ion migration in the pore fluid and ion diffusion under the electric field force, respectively. The term $L(\omega)\frac{\partial P}{\partial z}$ is the electric current produced by the pressure field in the pore fluid, and $L(\omega)$ is defined as the seismoelectric coupling coefficient (C_{sp}).

The radius in the capillary model is $r_0 = \sqrt{8k/\phi}$, which is obtained by solving Equation (1) and Equation (2) to eliminate n_0 (i.e., $n_0 = \frac{\phi}{\pi r_0^2} = \frac{\phi^2}{8k\pi}$). Now, recalling, $K = \sqrt{\frac{i\omega\rho_f}{\eta}}$, $d = \sqrt{\frac{\varepsilon k_B T}{2e^2Z^2n_A C_0}}$, and the ion concentration distribution from Equation (12) and (13), combining Equation (28) and Equation (29) we have

$$\alpha = 2\pi e n_A Z^2 \frac{\phi^2}{8k\pi}\left[\int_0^{\sqrt{8k/\phi}} (v_+C_+ - v_-C_-) rdr\right] \tag{31}$$

$$\beta = -2\pi e n_A Z \frac{\phi^2}{8k\pi}\left[\int_0^{\sqrt{8k/\phi}} \frac{(C_+ - C_-)\varepsilon\zeta}{\eta(1+K^2d^2)}\left[\frac{J_0(Kr)}{J_0(K\sqrt{8k/\phi})} - e^{\frac{\sqrt{8k/\phi}-r}{d}}\right] rdr\right] \tag{32}$$

The composite conductivity is

$$\sigma(\omega) = \alpha + \beta \tag{33}$$

The seismoelectric coupling coefficient can now be stated as

$$L(\omega) = -2\pi e n_A Z \frac{\phi^2}{8k\pi}\left[\int_0^{\sqrt{8k/\phi}} \frac{C_+}{i\omega\rho_f}\left[1 - \frac{J_0(Kr)}{J_0(K\sqrt{8k/\phi})}\right] \mathrm{rdr} - \int_0^{\sqrt{8k/\phi}} \frac{C_-}{i\omega\rho_f}\left[1 - \frac{J_0(Kr)}{J_0(K\sqrt{8k/\phi})}\right] rdr\right] \tag{34}$$

This equation is the expression of the streaming potential coupling coefficient in the frequency domain (Yu et al., 2013).

Table 2. Parameters used in this work for calculating the seismoelectric coupling coefficient.

Parameters	Values	Parameters	Values
Fluid Concentration c_0 (kg/dm^3)	1.5×10^{-3}	Fluid viscosity μ (Pa·s)	0.89×10^{-3}
Absolute temperature T (K)	298	Boltzmann constant k_B (J·K^{-1})	1.38×10^{-23}

Fluid density ρ_0 (kg/m^3)	1000.0	Fundamental charge e (C)	1.6×10^{-19}
Dielectric constant of water ε (F/m)	$80 \times 8.854187817 \times 10^{-12}$	Ionic valence (NaCl) Z	1

Note. The value for c_0 was measured in the laboratory. The values for ε are from Lide (2010).

Theoretical modelling results

The theoretical modelling carried out in this work uses a number of standard and experimental parameters which are given in Table 2. Figure 4 shows the seismoelectric coupling coefficient as a function of frequency, porosity and permeability derived from the theoretical treatment presented earlier and Equation (34) in particular.

We should know that there is a close relationship between porosity and permeability for real rocks. Permeability is dependent largely on the pore structure. Many empirical equations are proposed to estimate the relationship of permeability and porosity. One of the famous equations was presented as Kozeny-Carman equation (1937):

$$\mathrm{K} = \frac{\phi^2}{C(1-\phi)^2 S^2} \tag{35}$$

Where ϕ is porosity, c and S are the Kozeny-Carman constant and the specific surface area of solid phase, respectively. Hence, in fact, permeability cannot be discussed separately with porosity. In the capillary model, according to Equation (1) and (2), the relationship between the porosity and permeability is represented as

$$\frac{\phi}{\mathrm{K}} = \frac{8}{r_0^2} \tag{36}$$

Hence, the theory in this paper takes the relationship between the porosity and permeability into consideration. And we focused on one parameter for one time (separated analysis of the porosity and permeability) to investigate the impact of a single variable.

Figure 4a shows how the coupling coefficient is modelled to vary as a function of porosity and frequency. In the low frequency range, the coupling coefficient is independent of frequency, but decreases as the frequency increases in the high frequency range. The onset of the decrease (the transition frequency approximately at 7.5×10^4 Hz) seems to be dependent upon porosity as evidenced by a shift in the peak of the out of phase component coupling coefficient to lower frequencies as porosity decreases. However, this shift is small. The low-frequency value of coupling coefficient increases with porosity by almost one order of magnitude as the porosity increases from 15% to 45%.

Figure 4b shows how the coupling coefficient is modelled to vary as a function of permeability and frequency. When the frequency is less than the transition frequency (as indicated in Figure 4b), the curve for the lowest permeability (1×10^{-15} m^2) shows the smallest value of coupling coefficient, and coupling coefficient increases with increases of permeability. Consequently, if the capillary bundle model represents real rocks well, we would expect high permeability rocks to present higher seismoelectric coupling coefficients. In Figure 4b, we also observe that the increasing permeability shifts the coupling coefficient curves to the left (i.e., to lower frequencies). The theoretical modelling therefore clearly shows that the transition frequency of the coupling coefficient decreases with increasing permeability.

The transition frequency indicates the beginning of the transition for the seismoelectric coupling. The $L_{SE}(w)$ is constant up to the transition frequency above which it decreases, and the more permeable the sample is, the lower the transition frequency is. When below the transition frequency, the viscous force between the solid matrix and pore fluid are strong, so the relative movements of the pore fluid and solid matrix are small, the attenuation mechanism in this case are usually an average motion of the fluid relative to a solid phase, which is a macro-mode motion called global flow, and the attenuation of the wave is small, hence, the elastic-wave induced seismoelectric coupling is in a qusi-static state. Above the transition frequency, the inertia force of pore fluid makes its motion lag behind that of solid matrix, thus causing the attenuation of the wave. In this case, the attenuation mechanism that often occurs is the local flow or squirt flow mechanism. The non-equilibrium pore pressure induced by acoustic wave forces the pore fluid to move locally. This mechanism is the main reason for the attenuation of acoustic wave propagation in fluid-saturated media. Therefore, when the frequency is higher than the transition frequency, the seismoelectric coupling coefficient decreases rapidly.

(a)

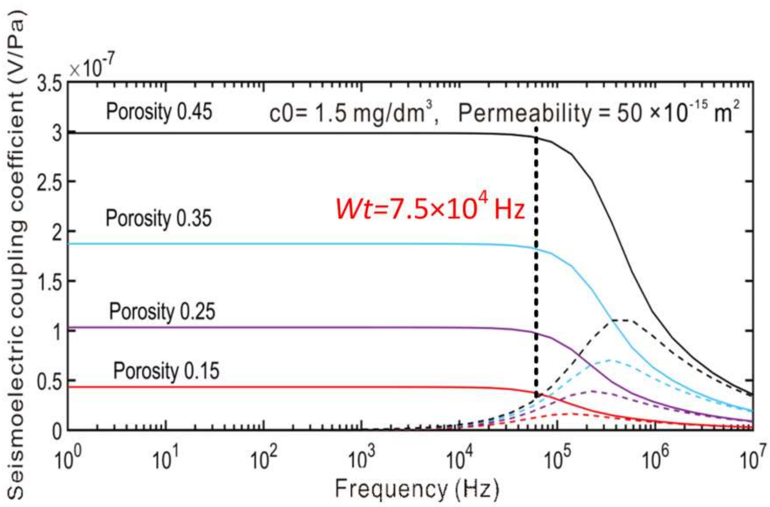

(b)

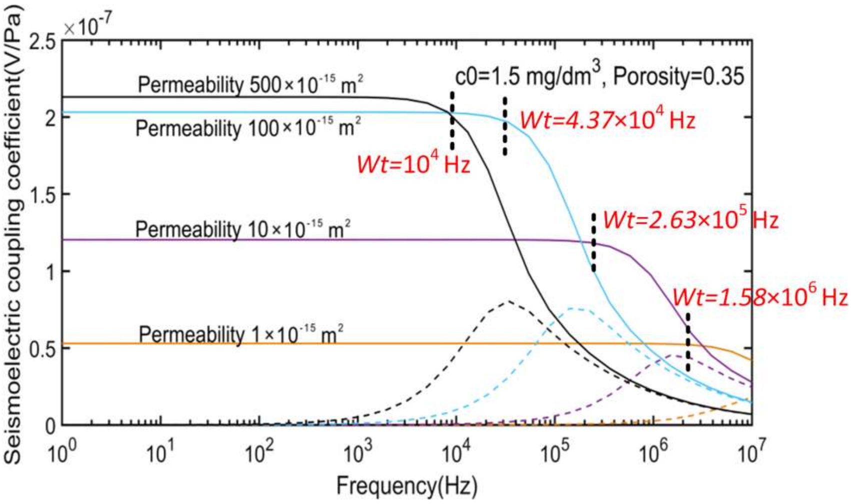

Figure 4. The modelled seismoelectric coupling coefficient $L(\omega)$ for the capillary bundle as a function of frequency, and (a) porosity, and (b) permeability, resulting in the application of the theoretical model for a capillary bundle developed earlier in this paper. The solid line and the dashed line show the real and imaginary portions of coupling coefficient, respectively.

From Figure 4a and 4b, we can see that the $L_{SE}(w)$ are independent with frequency (quasi-static) in a certain frequency range. And this frequency range is about 75 kHz in Figure 4a and 10 kHz in Figure 4b. The permeability of natural rocks are almost less than 500×10^{-15} m^2, so the quasi-static frequency range can be considered as 0-10 kHz when we combine the results of these two figures. That's why we define 0-10 kHz as the low frequency range and over 10 kHz as the high frequency range.

Figure 4a and 4b also present the imaginary parts of the seismoelectric coupling coefficient. We can see that the magnitudes of imaginary parts (dashed line) of $L_{SE}(w)$ change with the real parts (solid line). And the sudden change point of imaginary parts is also changes with the critical frequency of the real parts. However, the physical meaning of the imaginary contributions to the $L_{SE}(w)$ is not sure. But there are some indications. The generation of the streaming potential is based on the relative motion of the solid matrix and the pore fluid (the electric double layer). This means that the fluid velocity causes the streaming potential, which implies that the frequency dependence of the streaming potential coupling coefficient depends on the frequency dependence of the dynamic fluid permeability. The dynamic fluid permeability at low frequencies is controlled by viscous flow that is represented by the real part of the dynamic permeability. And after reaching transition frequency, the inertial acceleration begins to control the flow which is represented by the imaginary part of the dynamic permeability. Hence, the real and imaginary parts of the streaming potential coupling coefficient are affected by the same transition from viscous-dominated to inertial-dominated flow (Glover et al., 2012). Also, the attenuation of acoustic wave caused by the relative motion between fluid and solid can be described by the "resonance" mechanism. When the frequency is lower than the transition frequency, the wave propagation causes the vibration of the solid matrix, the fluid vibrates with the solid matrix only under the viscous force, which is almost the in-phase motion between fluid and solid matrix. In this frequency range, the imaginary part of the coupling coefficient is nearly zero. When the frequency increases more than the transition frequency, the effect of the inertial force of the fluid increases gradually, and the relative displacement between the fluid and the solid matrix occurs, this means that the vibration between the fluid and solid matrix is out of phase. The imaginary part of the coupling coefficients increases gradually, and the real part of the coupling coefficients decreases fastest when the imaginary phase of the coupling coefficients increases to the peak. This shows that the out-of-phase vibration between solid and fluid is strongest at this time. When the frequency continues to increase, the frequency of solid movement catches up with that of fluid, and the motion of solid and fluid gradually converges, and the out-of-phase vibration weakens, resulting in the imaginary phase of the coupling coefficient tending to zero, so the imaginary value of the coupling coefficient may represent the intensity of out-of-phase vibration between solid and fluid. Large imaginary phase of $L_{SE}(w)$ indicates the strong out-of-phase vibration and large attenuation of seismoelectric coupling.

A comparison of Figure 4a and Figure 4b shows that permeability seems to have larger influence on transition frequency than porosity. For seismoelectric transition frequency, Pride (1994) defined the transition frequency as

$$\omega_{\mathrm{t}} = \frac{\phi}{\alpha_{\infty} k} \frac{\eta}{\rho_f} \tag{37}$$

This transition frequency separates the low-frequency viscous flow regime from the high-frequency inertial flow regime. Porosity is given by ϕ, viscosity by η, tortuosity by α_{∞}, permeability by k and fluid density by ρ_f.

The capillary model implies that $\alpha_{\infty} = 1$, $\phi = n_0 \pi r_0^2$, $k = n_0 \pi r_0^4 / 8$ (Equation (1) and Equation (2), respectively). The transition frequency then becomes

$$\omega_t = \frac{8}{r_0^2} \frac{\eta}{\rho_f}, \tag{38}$$

which is consistent with the transition frequency of Walker and Glover (2010). Furthermore, a simple substitution of $\alpha_{\infty} = 1$ into Equation (37), the transition frequency ω_t becomes

$$\omega_t = \frac{\phi}{k} \frac{\eta}{\rho_f} \tag{39}$$

which is dependent on the porosity and permeability.

In addition, Jouniaux and Bordes (2012) analysed the transition frequency as a function of the permeability on various samples with parameters (porosity ϕ, intrinsic permeability k_0, formation factor F) measured from different authors, the predicted relationship between the transition frequency and permeability is

$$\log_{10}(\omega_t) = -0.78\log_{10}(k) - 5.5 \tag{40}$$

This equation is more practical since this relationship is based on actual measurements.

Because the transition frequency is a function of the capillary radius (Equation 38). Hence, we interpret to arise from the greater sensitivity of the permeability to capillary radius (by a factor of 4) than porosity (by a factor of 2) that can be confirmed by checking with Equation 1 and Equation 2. The difference in the sensitivity of the transition frequency to permeability rather than to porosity cannot in this case be attributed to the tortuosity of the pores as for our capillary model the tortuosity is high, constant and equal to unity. Plotting the modelled seismoelectric coupling coefficient transition frequency against permeability shows a very clear power law behaviour as evidenced by the negative gradient straight line on the log-log plot shown in Figure 5 (Equation (40)).

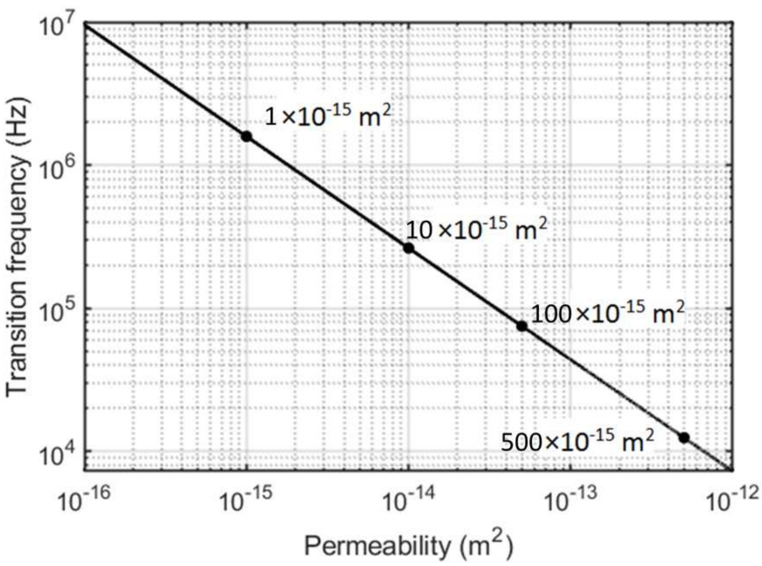

Figure 5. The modelled seismoelectric coupling coefficient transition frequency ω_t as a function of permeability.

We can see that the changes in transition frequency lead to the changes of the quasi-static range of $L_{SE}(w)$, especially according to the results in Figure 4b. When the frequency is lower than the transition frequency, the viscous force plays a leading role in the movement of fluid in porous media; when the frequency is higher than the transition frequency, the inertial force dominate the movement of fluid in porous media. The higher the permeability, the lower the transition frequency, the easier it is for fluid in pore media to change from laminar to inertial flow. If the transition frequency is invariable, the relationship between $L_{SE}(w)$ and permeability will be simple (monotonically increasing or decreasing), but the rapid change of conversion frequency with the increase of permeability results in the complexity of the change of the dependency of $L_{SE}(w)$ on permeability in frequency domain. As can be seen from Figure 7, the change of frequency will present different variation curves between the $L_{SE}(w)$ and permeability. At high frequencies, such as 100 kHz and 500 kHz, there will be a sudden change in the $L_{SE}(w)$ from increasing trend to decreasing trend. By knowing the relationship between transition frequency and permeability, we know what kind of permeability range the transition frequency of $L_{SE}(w)$ will appear, and what frequency we should choose to do the experiment to achieve the change of $L_{SE}(w)$ covering both the quasi-static range and the range after the transition frequency. Hence, for the experiment in the following part of this paper, we choose frequency in both low frequency range (1 kHz, 10 Khz) and high frequency range (500 kHz). However, we have not got the relationship of $L_{SE}(w)$ and permeability at the transition frequency because of the equipment limit (not enough experimental frequency range).

(a)

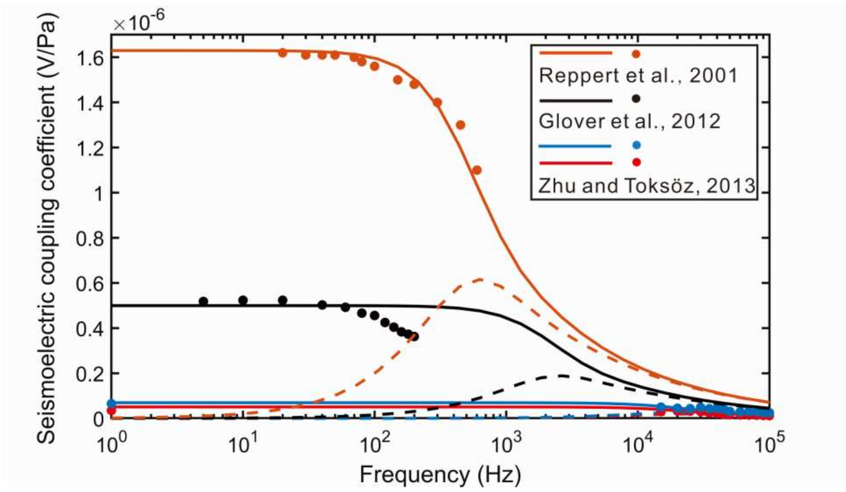

(b)

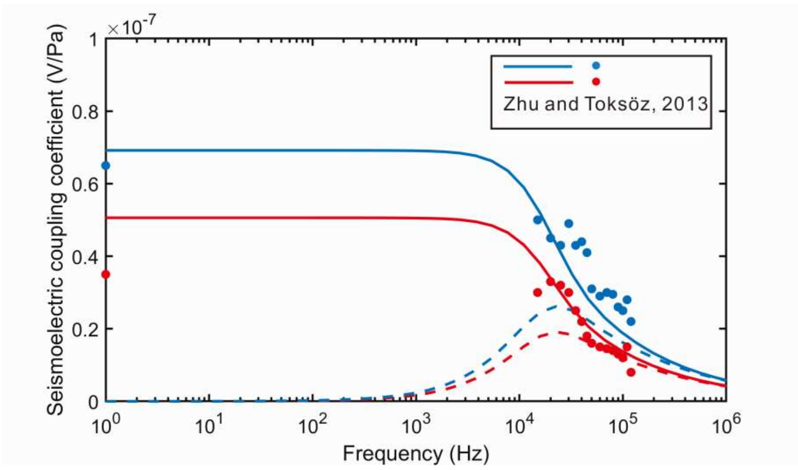

Figure 6. Comparisons between the measured published data of seismoelectric coupling coefficients and the theoretical curves in this paper (a) and the enlarged figure of the measured data from Zhu and Toksöz. The input parameters of the theoretical curves are from the corresponding published literature.

In Figure 6, the measured frequency-dependent seismoelectric coupling coefficients from Reppert et al. (2001), Glover et al. (2012) and Zhu (2013) are presented. Comparing these measured data with the theoretical curves in this paper, we found that in a wider frequency band (Glover et al., 5-200 Hz; Reppert et al., 20-600 Hz; Zhu and Toksoz, quasistatic and 15k-20 kHz), the measured points from Reppert's and Zhu's data are consistent with the theoretical curves, and there is a small deviation between Glover's measured data and theoretical curves but within the error range. This indicates that the seismoelectric coupling theory based on capillary model in this paper is reliable.

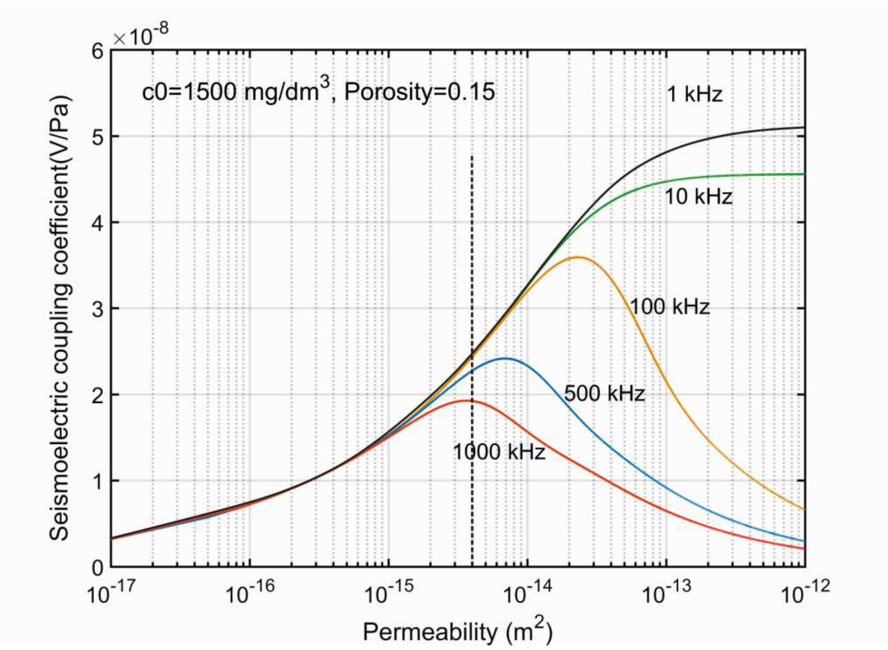

Figure 7. Modelled seismoelectric coupling coefficient $L(\omega)$ for a capillary bundle as a function of permeability for a range of different frequencies.

Figure 7 shows how the modelled seismoelectric coupling coefficient varies with permeability for different frequencies. One obvious characteristic of the curves is that the pattern of the variation of the seismoelectric coupling coefficient with permeability changes with frequency. For frequencies of 1 kHz and 10 kHz with a porosity of 15%, the seismoelectric coupling coefficient increases as the permeability increases, with the rate of increase being fast in the low permeability range (less than 100×10^{-15} m^2) and becoming slower in the high permeability range (over 100×10^{-15} m^2), but with no sudden alteration in the rate of change of seismoelectric coupling coefficient with permeability. By contrast, for higher frequencies (100 kHz, 500 kHz, 1000 kHz), while the seismoelectric coupling coefficient increases for low permeabilities as before, the rate is the same until a particular value of permeability is reached whereupon the seismoelectric coupling coefficient changes its behaviour and decreases with any further increase in permeability. Consequently, there is a sudden alteration in the rate of change of seismoelectric coupling coefficient with permeability from positive permeabilities to negative at high permeabilities. The permeability values at which this occurs for all 3 frequencies modelled and shown in Figure 7 are 2.5×10^{-14} m², 7×10^{-15} m² and 4.05×10^{-15} m², respectively. The presence of a threshold between 2 different regimes of behaviour is, however, interesting. Below the permeability threshold shown by the vertical dashed line we have what are generally termed tight clastic and carbonate rocks and gas and oil shales, while above the threshold exist more conventional clastic and fractured carbonate reservoirs. The threshold represents the peak $L(w)$ for a frequency of 1000 kHz, and occurs at a permeability of 4.05×10^{-15} m^2 (4.05 mD). Since the frequency of seismic sources in field explorations are generally less than 1000 kHz, and becoming lower with propagation, it follows that rocks with permeabilities less than 4.05×10^{-15} m^2 (4.05 mD) will see an increase in $L(w)$ with permeability and those above this permeability will experience a decrease in $L(w)$ with permeability. Consequently, there is significantly different behaviour for unconventional reservoir rocks and conventional ones.

Experimental results

Seismoelectric pressure and voltage signal measurement

We acquired the seismoelectric conversion signals and acoustic signals of natural samples using the experimental apparatus shown in Figure 1. Figure 8 shows the measurements made in the experiment. Figure 8a and 8b shows the acoustic signals received at the two measurement ends of a selection of 7 sandstone samples with typical behaviour, each having a different permeability and each being measured at 10 kHz and 500 kHz, respectively. Sandstone samples have little or no effect on the acoustic signal acquired at the front interface of samples (P1), hence, the P1 of each rock sample is the same and are shown as the in-filled black line. After the *P*-waves propagate through the rock sample, there is both an amplitude decrease and a travel time delay on P2 due to the thickness of rock sample as shown by the red curves.

(a) **(b)**

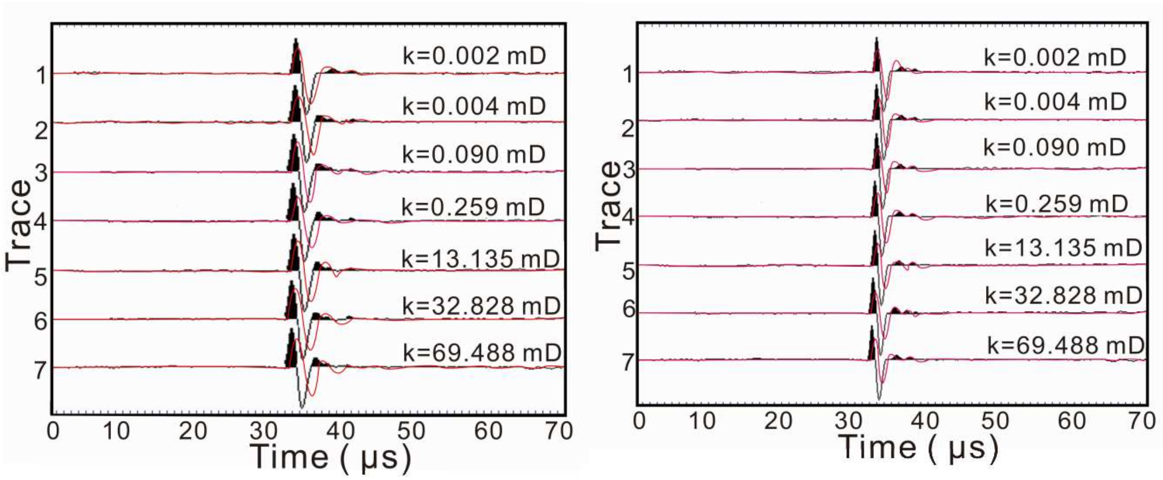

(c) **(d)**

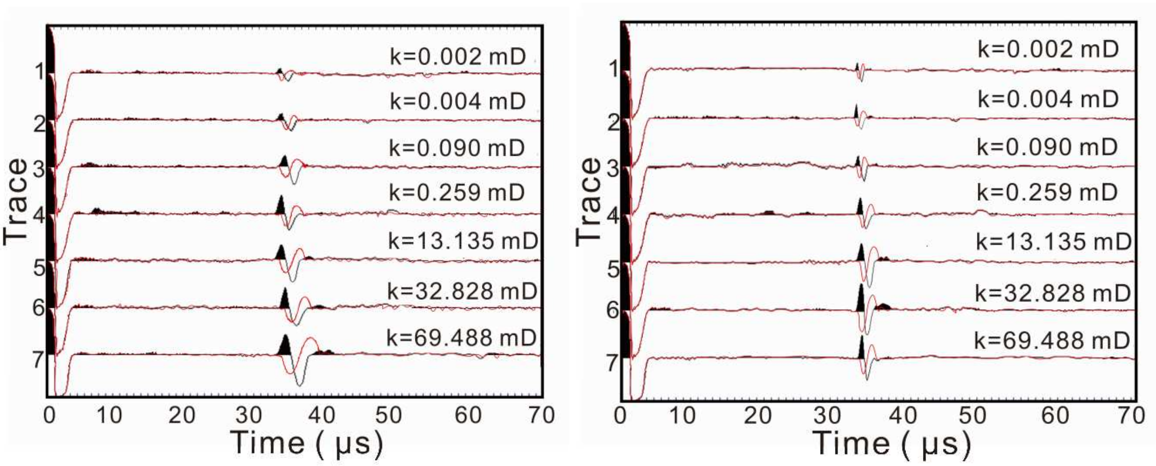

Figure 8. The acoustic signals and seismoelectric signals measured at the two sides of 7 sandstone samples from a total of 28 natural samples. Figure 8a and 8b represents the acoustic signals (P1 = black infilled and P2 = red), recorded at frequencies of (a) 10 kHz, and (b) 500 kHz. Figure 8c and 8d illustrates the seismoelectric potential signals of two electrodes (V1 = black infilled and V2 = red), recorded at frequencies of (c) 10 kHz, and (d) 500 kHz.

Figure 8c and 8d shows the electric signals of the same 7 natural sandstones recorded by two electrodes at the frequencies of 10 kHz and 500 kHz, respectively. We observe that the polarity of high voltage pulses at the start is the same, but the seismoelectric responses between 30 µs and 40 µs exhibit a polarity reversal of the seismoelectric signals received by the two electrodes. This phenomenon is in agreement with the experimental results of Zhu et al. (2008). The amplitudes of the seismoelectric signals received by V2 (red) is smaller than that collected by V1 (black); this is caused by the intrinsic attenuation of the wave propagation from the front side (V1) to the back side (V2) of the rock sample. Hence, the induced SE signals at the back side (V2) is smaller. There is also a short time delay between the signals because of the travel time in the propagation of P-waves in the rock sample. It can be seen that the amplitudes of the seismoelectric signals change with rock permeability.

It is also possible to note that the seismoelectric amplitude increases as the permeability increases for the frequency of 10 kHz (Figure 8c), but such an association is not clear for a frequency of 500 kHz in Figure 8d.

In the following subsections we present experimental results together with associated modelling. The results are presented first for the natural samples with porosities between 9.91% and 16.3%, and then for the artificial samples which have a tightly controlled, higher porosity of 23.8%. This has not been done because there is a particular difference in their behaviour, but to convenience the comparison of experimental results with experimental modelling.

Seismoelectric coupling coefficient of natural rock samples as a function of permeability

Figure 9 presents the relationship between the seismoelectric coupling coefficient and permeability for those samples with porosities varying between 9.91% and 16.3% (the porosities are showed in Table 1). Each of the parts of Figure 9 includes both measured data as symbols with error bars as well as bounding theoretical curves for the highest and lowest porosity in the dataset, which were obtained by applying our capillary bundle model for the bounding porosities. Figure 9a represents behaviour in the low frequency range and the measurements were made at 10 kHz. The theoretical value of the seismoelectric coupling coefficient increases with permeability throughout the range of permeabilities. The rate of increase of seismoelectric coupling coefficient is fast in the very low permeability range and becomes smaller at higher permeabilities. It is instructive to note that almost all the experimentally measured values fall within the envelope formed by the theoretical curves. This indicates that the experimental results are generally consistent with the theoretical trend. Figure 9b shows the theoretical and experimental data in the high frequency range (500 kHz). In this case the seismoelectric coupling coefficient first increases as permeability increases, reaches a peak, then decreases as permeability increases further. Once again, the experimental data generally falls within the envelope provided by the modelling curves.

(a) (b)

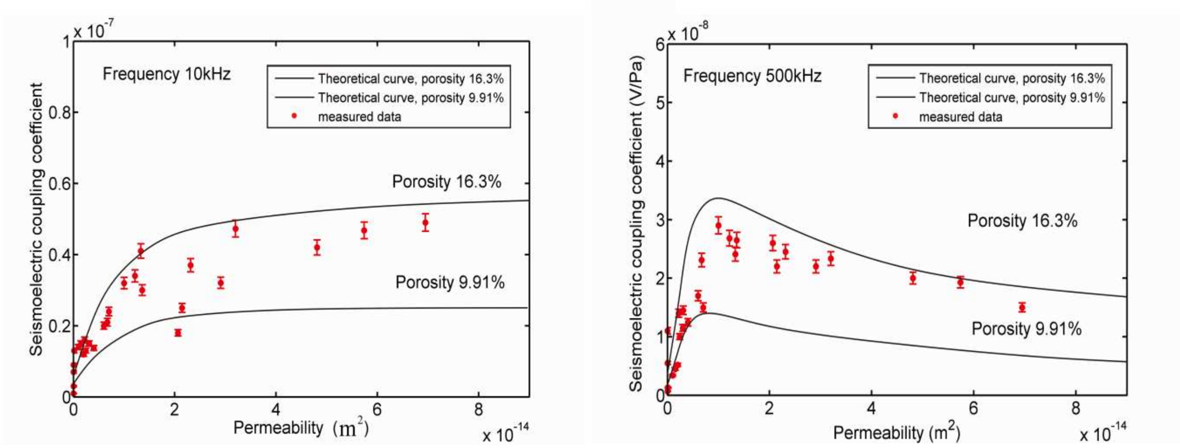

Figure 9. Seismoelectric coupling coefficient as a function of rock permeability for natural rock samples falling in the porosity range 9.91% to 16.3%, for measurements made at (a) 10 kHz, and (b) 500 kHz. The red symbols represent experimentally measured values of seismoelectric coupling coefficient ($L(\omega)$), and have error bars which are all about ± 5%, thanks to the stability of both the pressure and potential measurements. The black curves represent modelled seismoelectric coupling coefficient using the capillary bundle model developed in this work and represented by Equation (34).

Seismoelectric coupling coefficient of artificial samples as a function of permeability

Figure 10 shows the modelled seismoelectric coupling coefficient curve and experimental data for the artificial sandstones which all have a tightly controlled porosity equal to 23.8%. Once again we find that the seismoelectric coupling coefficient increases with the permeability at the frequency of 1 kHz (Figure 10a), the increase being fast at low permeabilities and becoming slower in the high permeability range. This behaviour is the same as for the natural rock samples at 10 kHz. For the data at 10 kHz (Figure 10b), the behaviour of the seismoelectric coupling coefficient on the 4 artificial sandstones is similar to that of natural rock samples measured at 500 kHz. The modelling curves would predict a very sharp increase of seismoelectric coupling coefficient with increasing permeability in the low permeability range, but these artificial samples have such a high porosity that none of them have such low permeabilities. However, in the higher permeability range, where we saw decreases in seismoelectric coupling coefficient with increasing permeability for the natural samples, we also get the same behaviour for the artificial samples. This same behaviour is continued when measurements are made at 500 kHz (Figure 10c), where once again there is no experimental data fitting into the initial very low permeability increases in seismoelectric coupling coefficient with permeability, but the higher permeability behaviour, which includes a significant drop in seismoelectric coupling coefficient with increasing permeability, sees the modelled curve once again matching the experimental data very well.

Interestingly, because all the samples share the same porosity, we can compare the experimental data with just one theoretical curve for that single porosity value, and all of the samples fall on or very close to the theoretical line, and in all cases within the error bars of the experimental measurements. This is a further validation of the use of a capillary bundle model for modelling the seismoelectric coupling coefficient of rocks, but also attests to the accuracy with which the experimental measurements were made.

(a) (b)

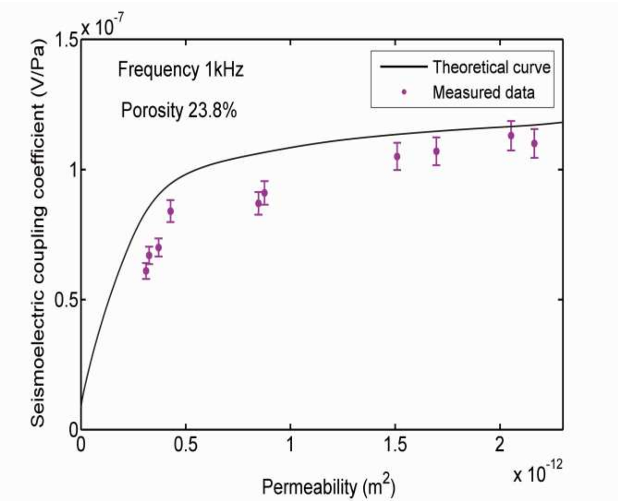

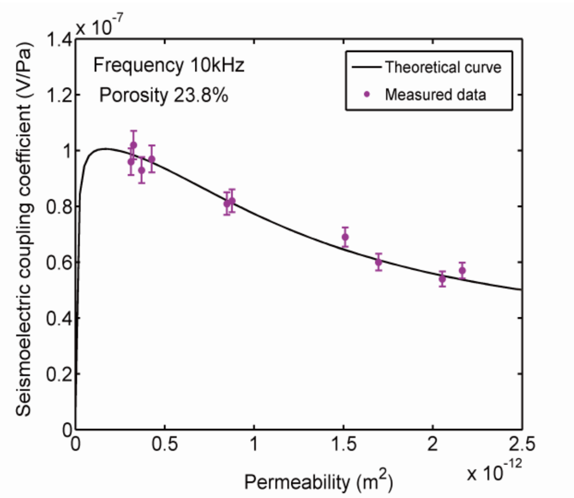

(c)

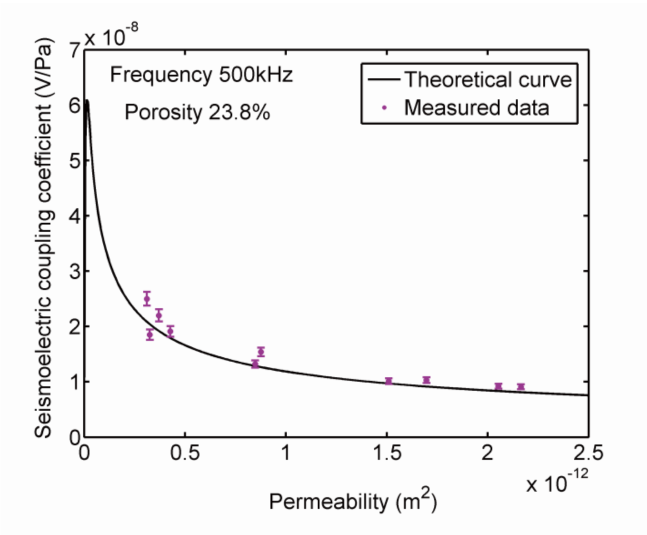

Figure 10 Seismoelectric coupling coefficient as a function of rock permeability for artificial rock samples with the porosity constrained to be equal to 23.8%, four measurements made at (a) 1 kHz, (b) 10 kHz, and (c) 500 kHz. The purple symbols represent experimentally measured values of seismoelectric coupling coefficient *L(w)*, and have error bars which are all about ± 5%, thanks to the stability of both the pressure and potential measurements. The black curves represent modelled

seismoelectric coupling coefficient using the capillary bundle model developed in this work and represented by Equation (34) for a porosity of 23.8%.

Discussion

The low permeability rock samples (natural rock samples) we used in this paper had a varying porosity. By contrast, the artificial sandstones all have the same, tightly controlled porosity. The permeability of these samples is very high. Consequently, we do not have experimental data of seismoelectric coupling for low-permeability samples, where the porosity is tightly controlled. Access to such data would allow us to confirm the analytical modelling curves of the *L(w)* variation in the low permeability range as we have done for the high permeability artificial samples in Figure 10. This is an important goal because the *L(w)* peak as a function of permeability and frequency occurs in the low permeability range.

The question arises why there is a sudden decrease of *L(w)* with further increasing permeability at high frequency (higher than 10 kHz). Most researches had previously indicated that seismoelectric conversion is enhanced as permeability increases (Jouniaux & Pozzi, 1995, 4 kHz; Mikhailov et al., 2000, 150 Hz; Zhu et al., 2015, 30 kHz). This is because a high permeability leads to a better flow, which can induce a larger relative displacement between the charges at the solid-fluid interface, and can then produce strong seismoelectric effects (Shaw, 1992; Pride, 1994; Haartsen & Pride, 1997; Haines et al., 2007). However, we found that the effect of permeability is to decrease the *L(w)* in the high frequency regime after it reaches a certain value. The higher the permeability, the smaller the *L(w)* in high frequency ranges. Shatilo et al. (1998) evaluated the ultrasonic attenuation on a set of rocks and found that the attenuation coefficient of *P*-waves in the water-saturated sandstones increases with permeability under high frequency (750 kHz). This indicates that in the case of high frequency, the higher the permeability, the greater the attenuation of *P*-waves. Therefore, the *P*-wave induced seismoelectric conversion in high-permeability rocks becomes weaker in high frequency range (Figure 7, Figure 9b, Figure 10b and Figure 10c).

In Figure 5, we can see that the transition frequency decreases with the increase of permeability. When the frequency is larger than the transition frequency, the inertia force plays a dominant role in fluid flow. This shows that when the transition frequency decreases, leading a decrease in the corresponding frequency at which the inertial forces start to play a dominant role in fluid. And this also means that the inertia force is easier to dominate fluid flow. In this case, the fluid flow caused by inertia force at high frequency belongs to squirt flow, which is the main cause of large-scale *P*-wave attenuation (Mavko & Jizba., 1991; Mavko et al., 2009; Dovorkin et al., 1994, 1995). Hence, permeability, transition frequency and attenuation are inseparable. With the increase of permeability, the transition frequency decreases, and the attenuation of P-wave increases, which weakens the seismoelectric conversion.

As can be seen from the comparison between the experimental results and the theoretical results in Figure 9 and 10, the experimental data points and the theoretical curves are not completely consistent, mainly because of the errors in both experiments and theoretical simulation. Although we want to minimize the errors in the study, the measurement errors of the experimental results are unavoidable, and the simulation of the theoretical model is very difficult to achieve complete agreement with the actual rock. Therefore, we consider that the small deviation between theoretical and experimental results is reasonable.

The theory of seismoelectronic coupling based on capillary model in this paper is only applied to the medium of single-phase saturated fluid, without considering the case of multi-phase fluid. Jackson (2008, 2010) used the capillary model to study the seismoelectric coupling theory of multi-phase fluid, but the results were quasi-static theory analysis, and the seismoelectric coupling coefficient is a function of saturation. The relation of $L(w)$ and permeability was not discussed in detail. For unsaturated case, Boarders et al. (2015) also studied the effect of water saturation on seismoelectric conversion based on the amplitudes ratio of seismic and seismoelectric waves. Although considering the situation of unsaturated media, they did not focus on the effect of permeability on seismoelectric coupling.

In the expression of seismoelectric coupling coefficient in Pride theory (Pride, 1994), the tortuosity (α_∞) and a porous-material geometry term (Λ) which contained in the dimensionless number m are difficult to determine, and the relationship between seismoelectric coupling coefficient and permeability is not intuitive. The theory in this paper is not compared with the seismic-electric coupling coefficient in Pride theory because of the differences of input parameters. The error of parameter determination may lead to great divergence between the two theories. The comparison of the two theories still needs to be further discussed in detail in future work.

Seismoelectric phenomena reveal the coupled properties that link the passage of seismic waves, fluid flow, porosity and permeability of reservoir rocks. And pore fluid permeability is commonly used in the characterization of reservoir rocks, any relationship between them would be useful (Glover & Jackson, 2009). The relationship might calculate the permeability of a rock from a seismoelectric measurement without recourse to empirical data-fitting (Glover et al. 2006). The derived seismoelectric coefficient in this paper reflects the relationship between the intensity of seismoelectric conversion and rock properties (porosity and permeability). In addition, measurements on natural and artificial samples, low permeability and high permeability samples have confirmed the validity of the theoretical relationship presented in this work. Consequently, this theoretical model may provide a template for seismoelectric exploration to predict the reservoir permeability, that is, the reservoir permeability could be deduced if the seismoelectric coupling coefficients can be measured downhole.

Conclusions

We have investigated the effects of permeability and porosity on the seismoelectric conversion using both experimental measurements and theoretical analysis. We measured the seismoelectric conversion using 28 rock sample samples with porosities in the range 9.91% to 16.3% and 4 artificial sandstones with constant porosity equal to 23.8%. We have also developed and implemented the capillary bundle model to calculate the seismoelectric coupling coefficient as a function of porosity, permeability and frequency theoretically. Experimental and theoretical analyses show that both porosity and permeability affect seismoelectric conversion and present a quantitative dependence between permeability and the seismoelectric coupling.

Both experimental and theoretical analyses of seismoelectric coupling indicate that seismoelectric conversion is stronger for high porosity rocks across a wide frequency range. But the effects of permeability on seismoelectric coupling are complex and can be divided into two permeability regions where 4.05×10^{-15} m^2 (4.05 mD) is the permeability demarcation point, below this permeability value (unconventional reservoir), the seismoelectric coupling enhances with the increase of permeability; and over this value (conventional reservoir), the seismioelectric coupling increases first and then decreases with the increase of permeability. In addition, the dependency of permeability on the seismoelectric coupling is different for different frequency range. At low frequencies (1 kHz) both the natural and artificial samples show that seismoelectric conversion is enhanced by increases in permeability, with the greatest sensitivity in the lower frequency range. At higher frequencies (10 kHz-500 kHz) there is a great increase in seismoelectric conversion with increasing permeability, but the seismoelectric conversion reaches a peak and then declines rapidly, especially at the higher frequencies. The quantitative relationship between permeability and the seismoelectric coupling is dependent on the frequency and permeability range, based on this quantitative relationship, the permeability can be inferred by the seismoelectric conversion.

The comparison of all the theoretical curves and measured data indicate that theoretical capillary bundle model developed in this work has been implemented and found to match the experimental data of natural and artificial samples very well. The curve was in very good agreement with the experimental data at all three frequencies from 1 kHz to 500 kHz. The sensitivity of seismoelectric coefficient increasing in permeability at low permeability raises the possibility that these changes might lead to a method for obtaining the permeability of reservoirs with low permeabilities such as tight oil in tight gas and shale gas reservoirs.

Acknowledgements

The study is supported by the China National Science & Technology Major Project (No. 2016ZX05007-006).

References

Alkafeef, S. & Alajmi, A., 2006. Streaming potentials and conductivities of reservoir rock cores in aqueous and non-aqueous liquids, *Colloids Surf. A*, **289**, 141–148.

Bockris, J. O. & Reddy, A. K. N., 1970. Modern electrochemistry: An introduction to an interdisciplinary area. *Plenum Press*, Vol. 1.

Bordes, C., Jouniaux, L., Garambois, S. & Dietrich, M., 2009. Seismoelectric and seismomagnetic measurements: original experiments within the low noise underground laboratory of rustrel (france) (invited), *American Geophysical Union, Fall Meeting 2009*, abstract id. NH31C–1123.

Bordes, C., Sénéchal, P., Barriére, J., Brito, D., Normandin, E., & Jougnot, D., 2015. Impact of water saturation on seismoelectric transfer functions: a laboratory study of coseismic phenomenon, *Geophys. J. Int*., **200**(3), 1317–1335.

Carman, P., 1937. Fluid flow through a granular bed, *Transactions of the Institution of Chemical Engineers*, **15**, 150–167.

Deissler, R. G., 1976. Derivation of the Navier–Stokes equation, *American Journal of Physics*, **44**(11), 1128–1130.

Ding, P., Di, B., Wei, J., Di, X. & Li, X., 2013. Construction and experiments of synthetic sandstones with controlled fracture parameters, *75th EAGE Conference & Exhibition Incorporating SPE EUROPEC*.

Ding, P., Di, B., Wei, J., Li, X. & Deng, Y., 2014a. Fluid-dependent anisotropy and experimental measurements in synthetic porous rocks with controlled fracture parameters, *Journal of Geophysics and Engineering*, **11**(1): 4905–4909.

Ding, P., Di, B., Wang, D., Wei, J. & Li, X., 2014b. P and S wave anisotropy in fractured media: experimental research using synthetic samples, *Journal of Applied Geophysics*, **109**, 1–6.

Dullien, F., 1979. Porous Media, Fluid Transport and Pore Structure, Elsevier, New York.

Dupuis, J. C., Butler, K. E., Kepic, A.W. & Harris, B. D., 2009. Anatomy of a seismoelectric conversion: measurements and conceptual modeling in boreholes penetrating a sandy aquifer, *Journal of Geophysical Research Solid Earth*, **114**(B10).

Dvorkin, J., Nolen-Hoeksema, R. & Nur, A., 1994. The squirt flow mechanism: macroscopic description, *Geophysics*, **59**, 428–438.

Dvorkin, J., Mavko, G. & Nur, A., 1995. Squirt flow in fully saturated rocks, *Geophysics*, **60**(1), 97–107.

Fiorentino, E. A., Toussaint, R. & Jouniaux, L., 2016. Lattice boltzmann modelling of streaming potentials: variations with salinity in monophasic conditions, *Geophysical Journal International*, **205**(1), ggw041.

Glover, P. W. J., Zadjali, I. I. & Frew, K. A., 2006. Permeability prediction from MICP and NMR data using an electrokinetic approach, *Geophysics*, **71**(4), F49–F60.

Glover, P. W. J. & Jackson, M. D., 2009. Borehole electrokinetics, *The Leading Edge*, **29**(6), 724–728.

Glover, P. W. J. & Déry, N., 2010. Streaming potential coupling coefficient of quartz glass bead packs: Dependence on grain diameter, pore size, and pore throat radius, *Geophysics*, **75**(6), F225–F241.

Glover, P. W. J., Walker, E., Ruel, J. & Tardif, E., 2012a. Frequency dependent streaming potential of porous media—Part 2: Experimental measurement of unconsolidated materials, *Int. J. Geophys.*, **2012**, 1–17.

Glover, P. W. J., Walker, E. & Jackson, M.D., 2012b. Streaming-potential coefficient of reservoir rock: A theoretical model. *Geophysics*, **77**(2), D17–D43.

Glover, P. W. J., 2018. Modelling pH-dependent and microstructure-dependent streaming potential coefficient and zeta potential of porous sandstones, *Transp Porous Med.*, 1573–1634.

Guan, W., Hu, H. & Wang, Z., 2013. Permeability inversion from low-frequency seismoelectric logs in fluid-saturated porous formations, *Geophysical Prospecting*, **61**(1), 120–133.

Haartsen, M. W. & Pride, S. R., 1997. Electroseismic waves from point sources in layered media, J. Geophys. Res., 102(1022), 24745–24784.

Haines, S. H., Pride, S. R., Klemperer, S. L. & Biondi, B., 2007. Seismoelectric imaging of shallow targets, Geophysics, 72(2), G9–G20.

Harris, S., 1971. An introduction to the theory of the Boltzmann equation, *Journal of Theoretical Biology*, **234**(1), 123–131.

Jackson, M. D., 2008. Characterization of multiphase electrokinetic coupling using a bundle of capillary tubes model, *J. Geophys. Res.*, **113**, B04201.

Jackson, M. D., 2010. Multiphase electrokinetic coupling: Insights into the impact of fluid and charge distribution at the pore scale from a bundle of capillary tubes model, *J. Geophys. Res.*, **115**, B07206.

Jougnot, D., Rubino, J. G., Carbajal, M. R., Linde, N. & Holliger, K., 2013. Seismoelectric effects due to mesoscopic heterogeneities, *Geophysical Research Letters*, **40**(10), 2033-2037.

Jouniaux, L. & Pozzi, J. P., 1995. Permeability dependence of streaming potential in rocks for various fluid conductivities, *Geophys. Res. Letters.*, **22**, 485–488.

Jouniaux, L., Bernard, M. L., Zamora, M. & Pozzi, J. P., 2000. Streaming potential in volcanic rocks from Mount Peleé, *J. Geophys. Res.*, **105**, 8391–8401.

Jouniaux, L., & Bordes, C., 2012. Frequency-dependent streaming potentials: a review. *International Journal of Geophysics*, **2012**, 1-11.

Klinkenberg, L. J., 1941. The permeability of porous media to liquids and gases. *Drilling & Production Practice*, **2**(2), 200-213.

Kozeny, J., 1927. Uber kapillare Leitung der Wasser in Boden, *Sitzungsber.Akad. Wiss. Wien*, **136**(2a), 271–306.

Lide, D. R., 2010. *CRC Handbook of Chemistry and Physics*, 90th edn (Internet), CRC Press.

Luong, D. T. & Sprik, R., 2013. Streaming potential and electroosmosis measurements to characterize porous materials, *ISRN Geophys*., **2013**, 1–8.

Mavko, G. & Jizba, D., 1991. Estimating grain-scale fluid effects on velocity dispersion in rocks, *Geophysics*, **56**(12), 1940–1949.

Mavko, G., Mukerji, T. & Dvorkin, J., 2009. *The rock physics handbook : tools for seismic analysis of porous media*, granular media.

Mikhailov, O. V., Queen, J. & Toksöz, M. N., 2000. Using borehole electroseismic measurements to detect and characterize fractured (permeable) zones, *Geophysics*, **65**(1), 1098–1112.

Morgan, F. D., Williams, E. R & Madden, T. R., 1989. Streaming potential properties of westerly granite with applications, *Journal of Geophysical Research Solid Earth*, **94**(B9), 12449-12461.

Pengra, D. B., Li, S. X. & Wong, P. Z., 1999. Determination of rock properties by low-frequency ac electrokinetics, *Journal of Geophysical Research Solid Earth*, **104**(B12), 29485–29508.

Peng, R., Wei, J. X., Di, B. R., Ding, P. B. & Liu, Z. C., 2016. Experimental research on seismoelectric effects in sandstone, *Applied Geophysics*, **13**(3), 425–436.

Peng, R., Di, B., Wei, J., Ding, P., Zhao, J., Pan, X. & Liu, Z. C., 2017. Experimental study of the seismoelectric interface response in wedge and cavity models, *Geophysical Journal International*, **210**, 1703–1720.

Pride, S. & Morgan, F. D., 1991. Electrokinetic dissipation induced by seismic waves, *Geophysics*, **56**(7), 914–925.

Pride, S., 1994. Governing equations for the coupled electromagnetics and acoustics of porous media, *Physical Review B Condensed Matter*, **50**(21), 15678.

Probstein R. F., 1994. *Physicochemical Hydrodynamics: An Introduction*, 1–8. Chemie Ingenieur Technik CIT.

Reppert, P. M., Morgan, F. D., Lesmes, D. P. & Jouniaux, L., 2001. Frequency-dependent streaming potentials, *Journal of Colloid & Interface Science*, **234**(1), 194–203.

Revil, A., Schwaeger, H., Iii, L. M. C. & Manhardt, P. D., 1999. Streaming potential in porous media: 2. Theory and application to geothermal systems, *Journal of Geophysical Research Solid Earth*, **104**(B9), 20033–20048.

Revil, A., Jardani, A., Sava, P. & Haas, A., 2015. The seismoelectric method. Chapter 2, John Wiley & Sons, Ltd.

Roubinet, D., Linde, N., Jougnot, D. & Irving, J., 2016. Streaming potential modeling in fractured rock: insights into the identification of hydraulically active fractures, *Geophysical Research Letters*, **43**(10).

Schakel, M. D., Smeulders, D. M. J., Slob, E. C. & Heller, H. K. J., 2011a. Laboratory measurements and theoretical modeling of seismoelectric interface response and coseismic wave fields, J. Appl. Phys., 109(7), 074903, doi:10.1063/1.3567945.

Schakel, M. D., Smeulders, D. M. J., Slob, E. C. & Heller, H. K. J., 2011b. Seismoelectric interface response: experimental results and forward model, *Geophysics*, **76**(4), N29-N36.

Schakel, M. D., Zhu, Z. & Smeulders, D. M. J., 2011c. Seismoelectric interface response—full-waveform model and measurements, in 73rd Eage Conference and Exhibition Incorporating Spe Europec, doi:10.3997/2214-4609.20149491.

Schakel, M. D., Smeulders, D. M. J., Slob, E. C. & Heller, H. K. J., 2012. Seismoelectric fluid/porous-medium interface response model and measurements,Transp. Porous Media, 93(2), 271–282.

Schoemaker, F., Smeulders, D. & Slob, E., 2007. Simultaneous determination of dynamic permeability and streaming potential, *SEG expanded abstracts*, **26**, 1555–1559.

Schoemaker, F., Smeulders, D. & Slob, E., 2008. Electrokinetic effect: Theory and measurement, *SEG Technical Program Expanded Abstracts*, 1645–1649.

Schoemaker, F., Grobbe, N., Schakel, M., Ridder, S. de., Slob, E. & Smeulders, D., 2012. Experimental validation of the electrokinetic theory and development of seismoelectric interferometry by crosscorrelation, *International Journal of Geophysics*, **2012**, 7-25.

Sénéchal, P. & Bordes, C., 2012. On the relevance of the acquisition configuration for seismoelectric recording, *EGU General Assembly Conference Abstracts*, **14**.

Shatilo, A. P., Sondergeld, C. & Rai, C. S., 1998. Ultrasonic attenuation in Glenn Pool rocks, Northeastern Oklahoma, *Geophysics*, **63**(2), 465–478.

Shaw, D. J., 1992. The solid-liquid interface, in Introduction to Colloid and Surface Chemistry, 4th edn, pp. 151–173, Butterworth-Heinemann.

Tardif, E., Glover, P. W. J. & Ruel, J., 2011. Frequency-dependent streaming potential of Ottawa sand, *Journal of Geophysical Research Solid Earth*, **116**(B4).

Thompson, A. H., Hornbostel, S., Burns, J., Tom, M., Robert, R. et al., 2007. Field tests of electroseismic hydrocarbon detection, *Geophysics*, **72**(72), 565.

Walker, E. & Glover, P. W. J., 2010. Permeability models of porous media: characteristic length scales, scaling constants and time-dependent electrokinetic coupling, *Geophysics,* **75**(6), E235–E246.

Walker, E., Glover, P. W. J. & Ruel, J., 2014. A transient method for measuring the DC streaming potential coefficient of porous and fractured rocks, *Journal of Geophysical Research: Solid Earth*, **119**(2), 957–970.

Walker, E. & Glover, P. W. J., 2018. Measurements of the Relationship between Microstructure, pH, and the Streaming and Zeta Potentials of Sandstones, *Transp Porous Med.*, **121**, 183–206.

Wang, J., Hu, H. S., Xu, X. R. et a1., 2010. Experimental measurement study on rock permeability based on the electrokinetic effect, *Chinese J. Geophys.*, **53**(8), 1953–1960.

Wang, J., Hu, H., Guan, W. & Li, H., 2015. Electrokinetic experimental study on saturated rock samples: zeta potential and surface conductance, *Geophys. J. Int*., **201**(2), 869–877.

Yu, H., Guan, J. T., Chen, H., Zheng, H. X. & Fang, W. J., 2013. Mathematical simulation on the frequency dispersion characteristics of the streaming potential in reservoir rocks, *Chinese Journal of Geophysics*, **56**, 676–687 (in Chinese).

Zhu, Z. Y., Toksöz, M. N. & Daniel, R. B., 2008. Electroseismic and seismoelectric measurements of rock samples in a water tank, *Geophysics*, **73**(5), E153–E164.

Zhu, Z. Y., & Toksöz, M. N., 2013. Experimental measurements of the streaming potential and seismoelectric conversion in berea sandstone, *Geophysical Prospecting*, **61**(3), 688–700.

Zhu, Z. Y., Toksöz, M. N. & Zhan, X., 2015. Seismoelectric measurements in a porous quartz-sand sample with anisotropic permeability, *Geophys. Prospect*., **64**, 700–713.